Efficient and Computationally Lightweight Design for MP6 Piezoelectric Micropump Flow Regulation Using Gain-Scheduled Fuzzy Logic Control

Tuan-Anh Vu [1], Quang-Dich Nguyen [2], Quang-Thong Trinh [2], Thanh Lam-Bui [1,*], and Thai-Viet Dang [2,*]

[1] School of Mechanical & Automotive Engineering, Hanoi University of Industry, Hanoi, 110000, Vietnam
[2] School of Mechanical Engineering, Hanoi University of Science and Technology, Hanoi, 112400, Vietnam
Email: anhvt_ck@haui.edu.vn (T.-A.V.); dich.nguyenquang@hust.edu.vn (Q.-D.N.); thong.trinhquang@hust.edu.vn (Q.-T.T.); buithanhlam@haui.edu.vn (T.L.-B.); viet.dangthai@hust.edu.vn (T.-V.D.)
*Corresponding author

***Abstract*—Piezoelectric micropumps such as the MP6 are widely used in portable and implantable microfluidic systems, where stable and accurate flow delivery is required under tight hardware constraints. Their coupled electro-mechanical and fluid dynamics, together with valve nonlinearities and viscosity changes, make fixed-gain linear control difficult to tune across the full operating range. This work develops a gain-scheduled fuzzy logic controller for the MP6 that uses flow error and its derivative as inputs, a compact 25-rule Mamdani structure, and gain factors obtained from open-loop characterisation at multiple flow rates. The controller is implemented on an STM32F4 microcontroller, and its timing and memory use are profiled. Closed-loop tests compare the fuzzy controller with a carefully tuned Proportional–Integral–Derivative (PID) controller over six flow setpoints from 13 to 700 µL/min and three working fluids: deionised water, a 10% glycerol mixture and phosphate-buffered saline. Performance is evaluated using settling time, overshoot, steady-state error and integral absolute error, with five repetitions per setpoint. Averaged over the six benchmarked setpoints from 13 to 700 µL/min, the fuzzy controller shortens settling time by about 33%, reduces overshoot by about 48% and lowers steady-state error and integral absolute error by roughly 42% and 31%, respectively, relative to PID. Stress-test operation at 800 µL/min, outside the benchmark range remained stable but showed increased oscillation, indicating the boundary of the current parameter set. These results indicate that gain-scheduled fuzzy control is a practical option for MP6-based drug-delivery and diagnostic systems within the tested flow and viscosity ranges and provide quantitative data to support future extensions to other micropump configurations.**

***Keywords*—piezoelectric micropump, fuzzy logic control, gain scheduling, flow control, real-time embedded systems**

I. Introduction

Recent advances in Micro-Electro-Mechanical Systems (MEMS) have accelerated the development and use of micropumps that underpin a wide range of microfluidic tasks [1]. These miniature devices enable on-chip analytics, biomedical instrumentation, and dose-controlled drug delivery at the microscale, where precise and stable flow regulation is essential [2]. Among actuation options, piezoelectric micropumps are attractive because they combine compact structure, low power demand, and inherent immunity to electromagnetic interference, which distinguishes them from electromagnetic drive schemes [3]. Their operation relies on the inverse piezoelectric effect: an applied electric field bends a piezoelectric diaphragm, changes the chamber volume, and generates net flow [4]. Small footprint, chemical compatibility, and high-resolution metering facilitate integration into portable and implantable systems [5]. Recent reports on piezoelectric silicon micropumps for drug delivery and related biomedical platforms illustrate this practical scope, while recent reviews summarise operating ranges and design trade-offs for piezoelectric micropumps [6]. Internal flow characteristics of valveless diffuser–nozzle designs have also been analysed in more detail in recent work [7].

Despite this progress, accurate flow regulation in piezoelectric micropumps remains challenging [8]. Closed-loop behaviour is governed by coupled electro-mechanical–fluidic dynamics and fluid–structure interaction. Architecture spans valved and valveless designs. In valved configurations, passive check valves are used to suppress backflow and increase volumetric efficiency, while valveless configurations employ diffuser–nozzle elements to bias pressure losses and generate net transport [9]. Inertial effects and threshold

Manuscript received December 23, 2025; revised February 2, 2026; accepted March 19, 2026; June 15, 2026.

behaviour in these elements introduce phase lag and transient backflow at higher drive frequencies, which can reduce efficiency and complicate controller design. Actuator configuration, including diaphragm material, thickness, and the choice between single-layer and bimorph structures, sets displacement and blocking force and therefore the achievable flow range [10].

In commercially available devices such as the MP6, several characteristics are of practical concern. All experimental work in this study was conducted on a commercial Bartels Mikrotechnik MP6 piezoelectric micropump module; details of the experimental hardware are provided in Section V.A. Piezoelectric actuation exhibits hysteresis and creep, so the diaphragm motion depends on voltage history rather than only the instantaneous command. Passive check valves introduce pressure-dependent thresholds and dead zones that vary with flow rate and fluid properties. The effective pump gain changes noticeably across the operating range from tens to hundreds of microlitres per minute because of the combined influence of valve dynamics, fluid compressibility, and membrane stiffness [11]. These nonlinearities mean that simple open-loop voltage–frequency schemes cannot maintain target flow over a broad range of operating points, so feedback control is required [12]. In practice, Proportional–Integral–Derivative (PID) control remains common because of its straightforward structure and established tuning rules. However, a single set of fixed gains cannot simultaneously give good performance at both low and high flow rates when the pump dynamics change with operating point. Gains that keep low-flow responses stable and free of overshoot often lead to sluggish behaviour at higher flows, while gains chosen for fast transients at high flows can cause oscillations near the lower end. Manual gain scheduling with discrete switching between parameter sets can mitigate some of these issues, but it increases calibration effort and may introduce transient disturbances at the switching points [13].

Within this context, fuzzy logic control offers a complementary approach that can address nonlinear behaviour without relying on a detailed mathematical model. Fuzzy logic controllers represent control policies as linguistic rules that relate input conditions to control actions, which helps account for threshold effects, hysteresis, and operating-point dependence observed in micropump systems. A Mamdani-type fuzzy controller with triangular membership functions and centroid (centre-of-area) defuzzification generates a continuous control surface from the error and error-rate signals. This smooth mapping can reduce chattering and avoid exciting structural modes in the piezoelectric diaphragm while remaining suitable for real-time implementation [14]. Recent studies in microfluidic manipulation have also shown that image-based fuzzy logic and related strategies can regulate droplet and pressure-driven flows in complex chip layouts [15–17]. These works, however, focus on other microfluidic platforms and do not examine the constraints imposed by commercial piezoelectric pumps with embedded actuation electronics.

Embedded platforms used with the MP6 impose additional constraints on control design. Model-predictive control, adaptive neuro-fuzzy inference, and sliding-mode control have been applied in other microfluidic and pumping contexts, but their online optimisation, high switching activity, or large memory requirements make direct implementation on low-cost microcontrollers difficult [18]. Under kilohertz-range actuation and millisecond-scale sampling, the control algorithm must run with deterministic timing and modest memory usage. A fuzzy controller with a small rule base and compact membership functions, implemented with centroid defuzzification, has computational complexity that scales approximately linearly with the number of active rules and allows partial pre-computation, which is favourable for resource-constrained embedded targets [19]. For the MP6 specifically, there is still limited documentation of gain-scheduled fuzzy controllers that are evaluated against carefully tuned PID baselines across multiple setpoints and working fluids, and whose timing and memory budgets are reported in a form directly useful for embedded-system designers [20].

This work addresses that gap by developing and validating a gain-scheduled fuzzy logic controller for the MP6 piezoelectric micropump with emphasis on implementation on a resource-constrained microcontroller. The controller uses a dual-input, single-output structure based on normalised flow error and its derivative, with compact triangular membership functions and a 25-rule base tuned for setpoint tracking and disturbance rejection. Gain scheduling adapts the effective control slope across the operating range using relationships identified from open-loop characterisation of the pump. The fuzzy controller is assessed through simulation and experiment against a PID controller that is tuned through a combination of classical rules and constrained numerical optimisation, so that the comparison reflects a realistic industrial baseline. The proposed gain-scheduled fuzzy controller is tailored to the MP6 and is shown to achieve stable closed-loop flow regulation. It improves transient behaviour and steady-state accuracy relative to a tuned PID benchmark over multiple flow setpoints and working fluids, and it is supported by engineering-level stability considerations under bounded parameter variations together with a quantified computational budget for real-time execution on an STM32F4-class embedded platform.

II. Related Work

Micropumps and microfluidic systems often exhibit strong operating-point dependence. Their dynamics are shaped by piezoelectric actuation, valve behavior, and fluidic loading. A range of nonlinear and data-driven control strategies has been reported for microfluidics. Fuzzy sliding-mode schemes improve robustness in bio-microfluidic manipulation, but the switching structure and tuning effort increase implementation burden [14]. Image-based fuzzy control has been used in droplet microfluidics to leverage visual feedback, yet it relies on a real-time imaging pipeline with high computational and power demands [15]. Reinforcement learning has been explored

for peristaltic microfluidic pumps and can optimize performance from data, but training cost and deployment complexity remain challenging for resource-limited embedded targets [17].

In the broader pumping literature, fuzzy control is frequently evaluated in simulation or industrial contexts. Simulation-focused comparisons between fuzzy logic control and PID can illustrate transient benefits, but they typically do not address deterministic timing and resource limits required by embedded real-time systems [8]. Industrial pumping-station studies emphasize operational stability and integration, and therefore place less emphasis on low-power microcontroller constraints [9]. Fuzzy methods have also been reported for parameter estimation or simulation-based drug-delivery analysis of micropumps, which supports system understanding but does not prioritize real-time closed-loop embedded validation [10, 11]. Closed-loop flow regulation for portable and implantable applications has been reported, highlighting the need for accurate control under tight energy budgets [12].

These studies indicate a gap at the intersection of advanced control and embedded feasibility. Many theoretically strong methods impose significant computational overhead or depend on heavy sensing pipelines, while many lightweight studies stop at simulation. Compact controllers that can adapt across operating conditions and that report timing and memory budgets are therefore important for practical deployment on microcontrollers [18–20].

Many closed-loop control studies for micropumps and microfluidic systems report improved tracking by exploiting robustness-oriented nonlinear control, model-based optimisation, or learning-assisted strategies [8, 14–18]. However, these approaches can require online computation, high-frequency switching, or additional sensing and signal processing, which complicates deterministic real-time implementation on low-cost microcontrollers under millisecond deadlines [18]. On the other hand, lightweight fuzzy-versus-PID comparisons often remain simulation-centric or do not report timing and memory budgets, making it difficult to judge practicality for embedded deployment [8, 9, 18–20]. For commercial MP6-class valved pumps in particular, studies that simultaneously cover a wide operating range, benchmark against a carefully tuned PID across multiple setpoints and working fluids, and quantify Microcontroller Unit (MCU) resource usage remain limited [20]. This motivates the present gain-scheduled Mamdani FLC designed from open-loop MP6 characterisation and validated experimentally with embedded profiling.

III. System Modeling and Analysis

A. MP6 Piezoelectric Micropump

Fig. 1 presents the MP6's architecture in a small, stacked construction driven by a piezoelectric element for precise dosing.

Fig. 1. Architecture of MP6 piezoelectric micropump.

The MP6 operates through a four-phase cycle (Fig. 2); piezo-driven diaphragm bending sets the flow direction: (a) Neutral state; (b) Left intake with right discharge; (c) Role reversal; (d) Cycle completion. Alternating chamber expansion and compression with passive check valves produces unidirectional flow.

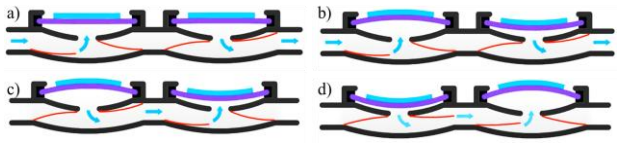

Fig. 2. The MP6's operating principle consists of 4 cycles. (a) The initial state, (b) The next phase, (c) The third phase, and (d) The final phase.

B. Dynamic Modeling

The internal actuation mechanism of the commercial MP6 module, illustrated schematically in Fig. 3, is treated in this work as a lumped input–output system. The control input is the drive voltage amplitude $V(t)$ delivered through the manufacturer's integrated driver circuit at a fixed actuation frequency; the output is the volumetric flow rate $Q(t)$ measured by the downstream flow sensor. No assumptions are made regarding the internal diaphragm geometry or actuator configuration, as these are not accessible in the sealed commercial module and are not required by the proposed controller.

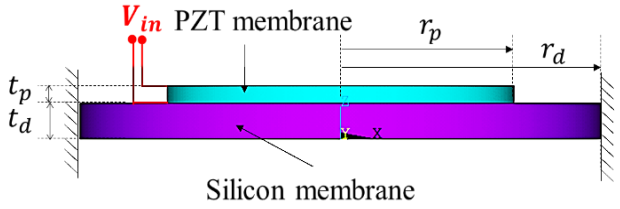

Fig. 3. Schematic of piezoelectric actuation mechanism.

For the purpose of post-design stability verification only, the pump is characterised by a nominal flow rate Q_{nom}, defined as the mean steady-state output measured during open-loop step-response tests at a given operating point. This empirical reference value replaces a derived theoretical flow term and is consistent with the black-box identification approach adopted throughout this study. The actual delivered flow rate Q_{actual} accounts for volumetric losses and valve inefficiencies according to:

$$Q_{actual} = Q_{nom} \times \eta_v \times \eta_c \quad (1)$$

where η_v represents the volumetric efficiency from 0.65 to 0.8 and η_c represents the check valve efficiency from 0.7 to 0.9. To ensure smooth operation, the valve flow is modeled using a continuous logistic function:

$$Q_{valve} = C_d A_v \sqrt{\frac{2\Delta P}{\rho}} \times \left[\frac{1}{1+e^{-k_v(\Delta P - P_{crack})}}\right] \quad (2)$$

where C_d is the discharge coefficient, A_v is the valve orifice area, ρ is the fluid density, ΔP is the pressure difference across the valve, P_{crack} is the valve cracking pressure, and k_v is the valve transition steepness parameter from 5 to 20 kPa^{-1}. The logistic formulation approximates the smooth transition from closed to fully open states, avoiding discontinuities that would complicate FLC while maintaining adequate fidelity to measured valve characteristics.

As for control system design, the relationship between input voltage amplitude and output flow rate is represented by a second-order transfer function Eq. (3). The aggregate input–output relationship between drive voltage amplitude and measured flow rate is represented by a second-order transfer function identified from open-loop frequency-response measurements conducted directly on the physical MP6 module:

$$\frac{Q(s)}{V(s)} = \frac{K_{pump}}{(1+\tau_1 s)(1+\tau_2 s)} \quad (3)$$

where:

$$K_{pump} = \frac{2A_{eff} k_p \omega \eta_v \eta_c}{\pi}$$

$$\tau_1 = \frac{V_0}{\beta A_{eff}} \text{ (fluid compression time constant)}$$

$$\tau_2 = \frac{L_{valve}}{A_v C_d}\sqrt{\frac{\rho}{2P_{avg}}} \text{ (valve response time constant)}$$

For controller synthesis and local verification, an empirical first-order approximation was used over the bandwidth relevant to closed-loop flow regulation. The approximation was based on the measured open-loop step response rather than on an algebraic combination of the fluid and valve time constants. This representation retains the dominant input–output behaviour needed for FLC tuning while avoiding unsupported assumptions about the sealed internal actuator structure. A recent 3D FSI study resolving diaphragm–valve interaction and fluid nonlinearities in valved piezoelectric micropumps is provided by Zhang *et al.* [21]. The equivalent transfer function is expressed as follows:

$$G_c(s) = \frac{K_c}{1+T_c s} \quad (4)$$

In Eq. (4), T_c denotes the empirically identified 63% open-loop step-response time constant at the corresponding operating point. It is not computed as $T_c = \tau_f + \tau_v/2$. From Eq. (4) onward, the local stability check uses normalized variables; therefore, Q, Q_{ref}, and the FLC output are mapped into dimensionless form before local gain analysis. The physical pump gain listed in Table I documents steady-state sensitivity, but it is not added directly to ω_n^2 in the normalized closed-loop characteristic equation. where $K_c = K_{pump} \times G_{norm}$ and $T_c = (\tau_1 + \tau_2)/2$, with G_{norm} being the normalization gain mapping the fuzzy controller output range $[1, -1]$ to the actual voltage range; model parameters are listed in Table I.

TABLE I. EQUIVALENT MODEL PARAMETERS FOR POST-DESIGN STABILITY VERIFICATION

Parameter	Symbol	Value	Unit
Piezoelectric sensitivity	k_p	50	μm/V
Maximum displacement	A	100	μm
Actuation frequency	ω	100	Hz
Nominal chamber volume	V_0	50	μL
Effective diaphragm area	A_{eff}	100	mm²
Discharge coefficient	C_d	0.65	-
Valve cracking pressure	P_{cr}	5	kPa
Fluid compression time constant	τ_f	5–20	ms
Valve response time constant	τ_v	2–10	ms

Parameters in Table I are identified from open-loop MP6 step-response tests or estimated from datasheet-level specifications. They do not entail access to MP6 internal geometry and are used solely in the verification framework of Section III.C.

C. Stability Analysis and Control Requirements

The simplified transfer-function model derived in Section III.B is used only for post-design verification. The gain-scheduled fuzzy logic controller is obtained from open-loop characterisation data and does not require an accurate global parametric model of the MP6. The analysis below therefore provides local engineering checks of stability and robustness over the tested operating range, rather than a formal global stability proof for the nonlinear closed-loop system.

(i) Local stability. Linearizing the FLC surface around $(e, \Delta e) = (0,0)$, yields effective gains shaped by rule activations. The effective proportional and derivative gains of the FLC surface at a given operating point are obtained by applying a central finite-difference approximation to the pre-computed lookup table of the controller output $\phi(e, \Delta e)$:

$$K_{p,eff} = \frac{\phi(\varepsilon,0) - \phi(-\varepsilon,0)}{2\varepsilon},\ K_{d,eff} = \frac{\phi(0,\varepsilon) - \phi(0,-\varepsilon)}{2\varepsilon} \quad (5)$$

where $\varepsilon = 0.02$ (normalised, dimensionless) is chosen to lie within the linear transition region of the PS/NS membership functions while remaining outside the flat core of the ZE trapezoid (±0.05). The resulting values, together with the gain-scheduled input scale factors K_e and $K_{\Delta e}$, are summarised at three representative operating points in Table II. At the nominal setpoint of 50∼L/min, this procedure yields $K_{p,eff} = 0.85$ and $K_{d,eff} = 0.042$.

TABLE II. LINEARISED FLC GAINS AT REPRESENTATIVE OPERATING POINTS (FINITE-DIFFERENCE, E = 0.02)

Q_{ref} (μL/min)	K_e	K_{de}	$\partial\phi/\partial e \Delta e \| 0$	$\partial\phi/\partial \Delta e \| 0$	$K_{p,eff}$	$K_{d,eff}$
13	0.308	0.068	1.12	0.28	1.10	0.058
50	0.200	0.050	1.12	0.28	0.85	0.042
300	0.082	0.026	1.12	0.28	0.62	0.031

$$K_{p,eff} = K_u \cdot \left(\frac{\partial \phi}{\partial e}\right) \cdot K_e \cdot K_{pump}$$

$$K_{d,eff} = K_u \cdot \left(\frac{\partial \phi}{\partial \Delta e}\right) \cdot K_{de} \cdot K_{pump}$$

The normalized FLC surface is fixed across operating points; only the input scaling factors vary with Q_{ref}according to the gain-scheduling law defined later in Section IV.D.

For the local stability check, the closed-loop dynamics were evaluated using the normalized first-order approximation in Eq. (4). Around a given operating point, the finite-difference gains $K_{p,\text{eff}}$ and $K_{d,\text{eff}}$ locally approximate the slope of the FLC surface. The corresponding normalized characteristic equation is written as:

$$\left(T_c+K_cK_{d,\text{eff}}\right)s+\left(1+K_cK_{p,\text{eff}}\right)=0.$$

Hence, the local pole is:

$$s=-\frac{1+K_cK_{p,\text{eff}}}{T_c+K_cK_{d,\text{eff}}}. \tag{6}$$

Since $T_c>0$, $K_c>0$, and the finite-difference gains remain non-negative within the tested operating domain, the local pole is real and negative. This result supports local operating stability of the normalized closed-loop model. The earlier second-order pole calculation is therefore not used because the physical pump gain and ω_n^2 are not dimensionally compatible without an explicit normalization path. At the nominal 50 µL/min point, substituting the values in Tables I and II into Eq. (6) yields a strictly negative real pole, confirming local asymptotic stability at the design centre.

(ii) Incremental gain analysis across the operating domain. To characterise controller behaviour beyond the local equilibrium without invoking formal absolute stability claims that would require a precise global plant model, an incremental gain scan was performed over the full normalised input domain. The partial incremental gains of the FLC surface $\phi(e,\Delta e)$ were evaluated numerically on a uniform 41×41 grid covering $e\in[-1,1]$ and $\Delta e\in[-1,1]$, including the output saturation boundary $|u|=1$:

$$g_e(e_i,\Delta e_j)=\frac{\phi(e_i+\varepsilon,\Delta e_j)-\phi(e_i-\varepsilon,\Delta e_j)}{2\varepsilon},$$
$$g_{\Delta e}(e_i,\Delta e_j)=\frac{\phi(e_i,\Delta e_j+\varepsilon)-\phi(e_i,\Delta e_j-\varepsilon)}{2\varepsilon} \tag{7}$$

with $\varepsilon=0.02$. The scan confirms that ϕ is Lipschitz continuous throughout the domain: the incremental gains remain bounded within $g_e\in[0,1.18]$ and $g_{\Delta e}\in[0,0.31]$, with no sign reversals observed. The minimum incremental gain is zero only at the saturation boundary and within the dead zone ($|u|<0.08$), where valve chatter suppression is intentional. These bounds provide engineering evidence consistent with closed-loop stability: the absence of sign reversals in $g_e$and $g_{\Delta e}$ across the full normalised domain rules out the class of destabilising slope reversals that would produce limit cycles under the first-order plant approximation of Eq. (4). Together with the normalized local-pole check in Section III.C(i) and the experimental margin results in Section III.C(iii), the incremental gain scan provides engineering evidence of stable local operation over the tested range. No claim is made regarding global nonlinear stability outside the calibrated domain.

(iii) Experimental confirmation. Fig. 4 summarises two views of the closed-loop stability verification. The Bode plot (panel a) is computed from the open-loop transfer function $L(j\omega)=K_{p,eff}\cdot G_c(j\omega)$ evaluated at the nominal operating point ($Q_{ref}=50$ µL/min, DI water), where G_c is the first-order approximation of Eq. (4) with parameters listed in Table I. At the nominal 50 µL/min operating point with deionised water, the Bode plot gives a gain margin of 12.3 dB and a phase margin of 48°, satisfying the nominal design thresholds of 6 dB and 48°. Margins at other operating points are reported in Table III and are interpreted as operating-condition-dependent verification results rather than uniform satisfaction of the nominal phase-margin target. Where phase margins fall below 48°—specifically at high flow rates with 10% glycerol—the experimental closed-loop responses in Section VI confirm bounded stable operation, providing empirical support that the reduced analytical margin remains practically sufficient within the tested range

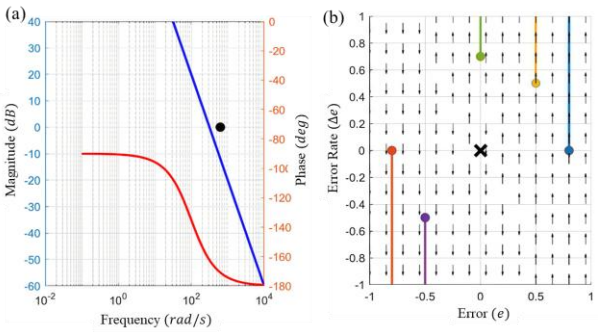

Fig. 4. Stability verification: (a) Bode margins confirming GM = 12.3 dB and PM = 48° at the nominal operating point; (b) phase portrait showing convergence from multiple initial conditions under the gain-scheduled FLC.

(iv) Robustness across operating conditions. Table III reports stability margins over 13–700 µL/min and for two fluids with ≈ 30% viscosity spread (deionized water, $\eta\approx1.0$ cP, vs. 10% glycerol, $\eta\approx1.3$ cP). The nominal 50 µL/min condition with deionised water satisfies the target margins. At higher flow rates and for the 10% glycerol mixture, the phase margin decreases as low as 35° at 700 µL/min with glycerol, indicating reduced but still positive stability margins. These points are therefore treated as reduced-margin operating conditions and are interpreted together with the bounded experimental responses reported in Section VI, rather than as full compliance with the nominal 48° phase-margin target.

(v) Real-time implementation requirements. The controller meets: sampling rate $f_s\geq1$ kHz; typical computation latency <100 µs per cycle (worst-case 142 µs when all 25 rules are active); actuator bandwidth >200 Hz; sensor esolution <1 µL/min; drive range 0–100 V at 12-bit; and FLC memory footprint ≈ 8 kB RAM. These constraints ensure deterministic timing on resource-

constrained microcontrollers; experimental validation is provided in Section V.

TABLE III. STABILITY MARGINS ACROSS OPERATING CONDITIONS

Flow (μL/min)	Deionized water ($\eta = 1.0$ cP) – GM (dB)	Deionized water – PM(°)	10% glycerol ($\eta = 1.3$ cP) – GM (dB)	10% glycerol – PM(°)
13	14.2 ± 0.8	52 ± 3	13.5 ± 0.9	48 ± 3
50	12.3 ± 0.6	48 ± 2	11.8 ± 0.7	38 ± 4
100	10.8 ± 0.7	43 ± 3	10.2 ± 0.8	40 ± 3
700	8.5 ± 1.2	38 ± 4	8.0 ± 1.2	35 ± 3

IV. FUZZY LOGIC CONTROLLER DESIGN

A. Overall Control Architecture

The FLC follows a dual-input, single-output scheme for MP6's flow regulation. The inputs are the normalized error e and the change in error Δe. After normalization, these signals are mapped by the FLC rule base to produce the voltage command u to the actuator. The mapping is tailored to the nonlinearity of the piezoelectric element and to the dynamics of the check valve. Consequently, the output adapts across operating conditions without an exact mathematical plant model. The structure is compact and clear, supporting straightforward experimental deployment.

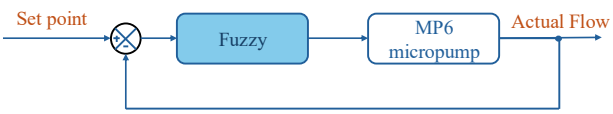

Fig. 5. Fuzzy controller block design.

Fig. 5 presents the overall FLC block diagram, which comprises two input variables and one output variable.

B. Design Rationale and Practical Considerations

The fuzzy logic controller for the MP6 was shaped by an iterative process that combined simple open-loop tests with the limits of the embedded hardware. After the basic structure in Section III.A had been fixed, around fifty step responses were recorded over the flow range used in this study. These responses were not used to build a full parametric model, but they did reveal the main nonlinear features that the controller had to handle.

The asymmetric triangular membership functions used for the error input follow three qualitative regimes observed in these data. At low flow rates below about 30 μL/min, the passive check valves operate close to their cracking pressure, so small changes in drive voltage can produce relatively large flow variations and even oscillatory behaviour. In this region the error sets are placed more densely around zero, roughly between −0.4 and 0.4 in the normalised domain, so that the controller can make finer corrections. Between about 30 and 100 μL/min the input–output relation is closer to linear, and a coarser partition is sufficient. At higher flow rates valve dynamics and fluid inertia introduce noticeable phase lag; the positive large sets therefore extend further in the normalised range to provide anticipatory action for large positive errors. The resulting asymmetry directly reflects measured pump behaviour rather than an imposed symmetric convention.

The 25-rule base in Table IV implements a simple and consistent control policy. Rules on the main diagonal, where the error and its discrete derivative have the same sign, apply stronger control moves so that large deviations from the setpoint are removed quickly. Rules where the error and its rate differ in sign use milder consequences to avoid overshoot as the response approaches the target. This pattern was refined over about fifteen tuning iterations. After each iteration, overshoot, rise time, and settling time were checked at the nominal setpoint of 50 μL/min, with design targets of less than 5% overshoot, rise time below 0.8 s, and settling within 2 s. Only a small number of rules were modified at each step so that the final rule base remained compact and easy to interpret.

The gain-scheduling law used in this study was derived from tests at seven operating points spanning 13, 28, 50, 100, 300, 600, and 700 μL/min. The six setpoints listed above (13, 28, 35, 100, 600, and 700 μL/min) constitute the primary benchmark set used for all quantitative comparisons. An additional stress-test trial at 800 μL/min was conducted with the same FLC parameter set to characterise the upper operating boundary; because it lies outside the calibrated gain-scheduling range, its results are presented in Section VI.B as a boundary condition rather than a benchmark point and are excluded from the average improvement calculations. At each point the base fuzzy controller was run with multiplicative gains between 0.3 and 2.0, and the gain that minimised the integral absolute error without inducing visible oscillations was recorded. A power-law fit was then applied to these discrete values. Power-law fitting was chosen because it provides smooth variation of the effective slope with flow rate and requires only a small set of coefficients to be stored, which is convenient for implementation. This form gave a reasonable compromise between tracking accuracy at high flow rates and stability margins at low flows.

Several practical measures were adopted to ensure deterministic execution on the STM32F4 platform. Membership degrees are obtained from lookup tables with linear interpolation instead of direct evaluation of analytic expressions. Rule firing strengths use 16-bit fixed-point arithmetic with appropriate scaling, and floating-point operations are kept to a small set where they offer clear benefit. For defuzzification the centroid method is used, but the centroids of the output sets are precomputed and stored in ROM so that each cycle requires only weighted sums and one division. Taken together, these choices reduce the number of floating-point operations from roughly 180 to about 40 per control cycle and keep the measured execution time within the 100 μs budget reported, even when many rules are active. Overall, each element of the controller can be traced either to an observed feature of the pump or to a hardware constraint, which distinguishes the design from a purely trial-and-error fuzzy tuning approach.

C. Fuzzification

The primary input variables are mathematically defined as follows:

$$e(k) = \frac{Q_{ref}(k) - Q_{actual}(k)}{Q_{ref}(k)};\ \text{and}\ \Delta e(k) = \frac{e(k) - e(k-1)}{T_s} \quad (8)$$

where $e(k)$ represents the normalized flow rate error, $\Delta e(k)$ represents the error derivative, and T_s denotes the sampling period. Normalization ensures consistent controller behavior across the operating range.

The input scaling factors are chosen to reflect the MP6's dynamic characteristics:

$$K_e = \frac{1.0}{0.1 \times Q_{nominal}};\ \text{and}\ K_{de} = \frac{T_c}{0.05 \times Q_{nominal}} \quad (9)$$

where $Q_{nominal}$ = 50 µL/min represents the typical MP6 micropump operating flow rate and T_c = 10 ms represents the equivalent time constant derived from the dominant pole of the linearized plant model (Eq. (4)). These scaling factors ensure optimal sensitivity while preventing excessive controller activity due to the noise measurement.

The input membership functions utilize asymmetric triangular distributions designed to accurately represent the practical operating characteristics of micropump systems. In Fig. 6, each input variable is characterized by five linguistic terms: Negative Large (NL), Negative Small (NS), Zero (ZE), Positive Small (PS), and Positive Large (PL). The membership functions are optimally distributed to improve control precision around the operating point, with the following definitions:

$$\begin{cases} \mu_{\mathrm{NL}}(e) & = \mathrm{trimf}(e; [-1.0, -1.0, -0.4]) \\ \mu_{\mathrm{NS}}(e) & = \mathrm{trimf}(e; [-0.6, -0.2, 0.0]) \\ \mu_{\mathrm{ZE}}(e) & = \mathrm{trapmf}(e; [-0.1, -0.05, 0.05, 0.1]) \\ \mu_{\mathrm{PS}}(e) & = \mathrm{trimf}(e; [0.0, 0.2, 0.6]) \\ \mu_{\mathrm{PL}}(e) & = \mathrm{trimf}(e; [0.4, 1.0, 1.0]) \end{cases} \quad (10)$$

The memberships are asymmetrical (Fig. 7). MP6 micropump open-loop tests indicated a stronger response at very low flow (approximately 0 to 50 µL/min); therefore, partitions are densified near zero error to capture this sensitivity.

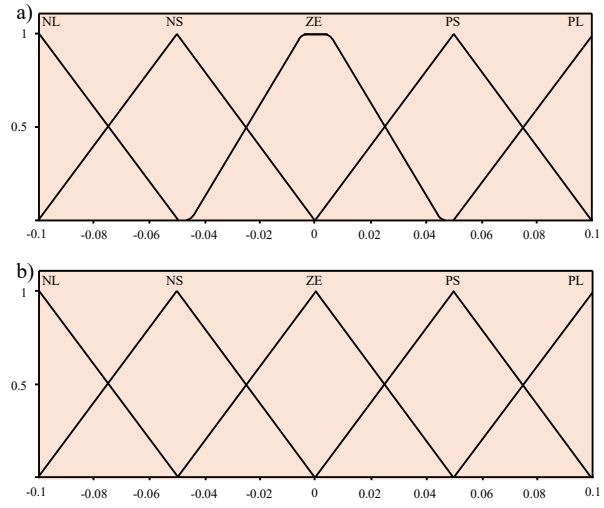

Fig. 6. Input membership function with (a): Flow error relative to setpoint (b): Flow error derivative.

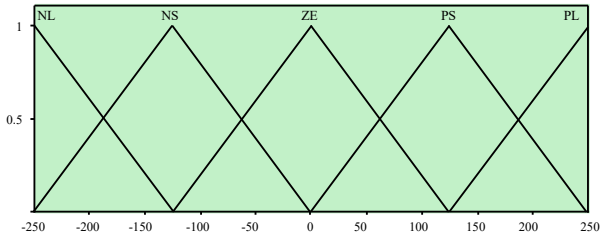

Fig. 7. Output membership function.

In Fig. 8, the FLC rule base consists of 25 carefully designed rules that incorporate MP6-specific control strategies. The 25-rule base (Table IV) implements anticipatory control: amplifying effort when error and its derivative share the same sign, attenuating near setpoint to prevent overshoot.

$$R1\text{: IF } e \text{ is NL AND } \Delta e \text{ is NL THEN } u \text{ is NL}$$

$$R13\text{: IF } e \text{ is ZE AND } \Delta e \text{ is ZE THEN } u \text{ is ZE} \quad (11)$$

$$R25\text{: IF } e \text{ is PL AND } \Delta e \text{ is PL THEN } u \text{ is PL}$$

TABLE IV. COMPLETE FUZZY RULE BASE

Δe	NL	NS	ZE	PS	PL
NL	NL	NL	NL	NS	ZE
NS	NL	NL	NS	ZE	PS
ZE	NL	NS	ZE	PS	PL
PS	NS	ZE	PS	PL	PL
PL	ZE	PS	PL	PL	PL

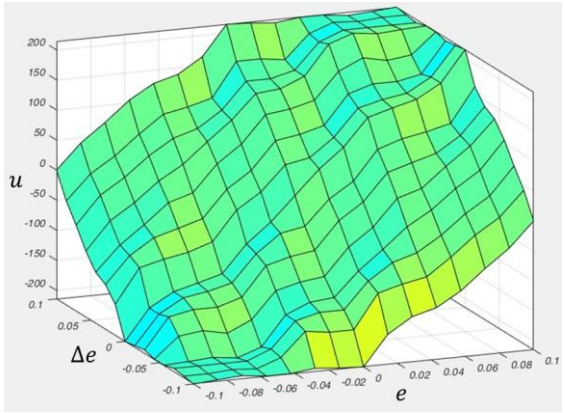

Fig. 8. Fuzzy rules' surface visualization showing smooth, continuous control mapping.

For inference, the antecedents are combined using the product t-norm:

$$\alpha_{ij} = \mu_{A_i}(e) \times \mu_{B_j}(\Delta e) \quad (12)$$

where α_{ij} represents the firing strength of rule R_{ij}. The aggregated output membership function is constructed through capped summation of individual rule contributions:

$$\mu_{output}(u) = min\left(1.0,\ \sum_{i,j} \alpha_{ij} \times \mu_{C_{ij}}(u)\right) \quad (13)$$

This aggregation method produces smooth output transitions while preventing abrupt voltage changes that could excite valve resonance or saturate the drive circuit.

Center of area defuzzification computes the crisp control output with enhanced precision:

$$u_{crisp} = \frac{\sum_{i,j} \alpha_{ij} \int u \mu_{C_{ij}}(u) du}{\sum_{i,j} \alpha_{ij} \int \mu_{C_{ij}}(u) du} \quad (14)$$

D. Gain Scheduling and Implementation

The control voltage generation incorporates bias compensation for the MP6 operating point:

$$V_{control}(k) = V_{bias} + K_u \times u_{crisp}(k) \quad (15)$$

where V_{bias} represents the steady-state voltage required for the MP6's nominal flow rate and $K_u = (Vmin_{max}$ provides appropriate scaling.

The FLC implements gain scheduling by adapting the input scaling factors K_e and K_{de} as functions of the commanded reference flow rate Q_{ref}. The scheduling variable is deliberately chosen as Q_{ref} rather than the measured flow Q_{meas} to avoid amplifying sensor noise into the gain computation, particularly at low flow rates where measurement uncertainty represents a larger fraction of the setpoint.

The scheduling laws were identified from open-loop step-response tests at seven operating points: 13, 28, 50, 100, 300, 600, and 700 ~ µL/min. At each point, the base FLC was operated with multiplicative input gains swept from 0.3 to 2.0, and the gain minimising integral absolute error without inducing sustained oscillation was recorded. A power-law model was then fitted to these discrete values:

$$K_e(Q_{ref}) = K_{e,nom} \times \left(\frac{Q_{nom}}{Q_{ref}}\right)^{0.5}, K_{de}(Q_{ref}) = K_{de,nom} \times \left(\frac{Q_{nom}}{Q_{ref}}\right)^{0.3} \quad (16)$$

The power-law fit yields coefficients of determination of $R^2 = 0.976$ for K_e and $R_2 = 0.961$ for K_{de}, with residuals remaining within ±0.08 across all seven calibration points, confirming that the two-parameter model captures the dominant trend without overfitting. At runtime, Q_{ref} is known exactly at the start of each control cycle from the setpoint register. The scaling factors are retrieved via a 16-point lookup table pre-computed at equally spaced values of $ln(Q_{ref}/Q_{nom})$ with linear interpolation in log-space, keeping the gain-scheduling overhead below 3 µs, as confirmed by the execution-time measurements.

Because the gain-scheduled FLC operates as a proportional–derivative mapping with no integrating element, integrator windup does not arise and no windup-compensation term is required. The sole protection mechanism is symmetric output clamping applied after the gain-scheduling multiplication:

$$V_{final}(k) = \text{sat}(V_{bias} + K_u \cdot u_{crisp}(k), V_{min}, V_{max} \quad (17)$$

where V_{min}~V and V_{max}~V correspond to the DAC drive limits. A dead zone of $|u_{crisp}| < 0.08$ is enforced upstream of the clamping stage to suppress valve chatter at near-zero error. The complete signal processing chain proceeds as follows: normalisation → rule-base inference → dead-zone suppression → bias addition → output clamping, with no feedback path from the clamping stage to any upstream block.

To verify the practical contribution of gain scheduling during controller implementation, a fixed-gain fuzzy controller was defined using the same 25-rule Mamdani base, inference engine, and defuzzification stage as the proposed controller. In this variant, $K_e$and $K_{\Delta e}$are held at their nominal 50 µL/min values, whereas the gain-scheduled controller updates both scaling factors according to Eq. (16). Table V reports this design-stage ablation check, which is used to justify the inclusion of gain scheduling in the final controller architecture. Values are reported as mean ± SD over five independent trials using the same protocol and performance metrics later applied in the PID–FLC benchmark. The last column reports the percentage reduction in IAE of FLC-GS relative to FLC-Fixed at the same setpoint.

TABLE V. DESIGN-STAGE ABLATION CHECK FOR GAIN SCHEDULING

Setpoint ($\mu L/min$)	Controller	Settling (s)	Overshoot (%)	SS Error (%)	IAE	Gain sched. benefit
13	FLC-Fixed	2.34 ± 0.19	9.2 ± 1.1	4.8 ± 0.6	28.7 ± 3.4	—
13	FLC-GS	1.52 ± 0.12	1.9 ± 0.3	1.6 ± 0.2	11.2 ± 1.5	↓ 61.0%
100	FLC-Fixed	2.41 ± 0.18	7.1 ± 0.9	3.8 ± 0.5	38.4 ± 4.6	—
100	FLC-GS	1.89 ± 0.15	4.5 ± 0.6	2.6 ± 0.4	32.1 ± 3.8	↓ 16.4%
700	FLC-Fixed	4.12 ± 0.33	18.4 ± 2.2	9.1 ± 1.1	115.6 ± 13.2	—
700	FLC-GS	2.58 ± 0.21	6.8 ± 0.9	4.1 ± 0.6	63.8 ± 7.6	↓ 44.8%

Note: Values are mean ± SD over five independent trials. Gain-scheduling benefit denotes the percentage reduction in IAE of FLC-GS relative to FLC-Fixed at the same setpoint. This design-stage ablation check is used to justify the gain-scheduling structure.

V. EXPERIMENTAL SETUP AND METHODOLOGY

A. Experimental System

Table VI presents the technical parameters of the equipment used in the experiment. Based on the proposed FLC, the experimental model for precise and stable control of MP6 is presented through the schematic diagram in Fig. 9(a) and the detailed structure of the basic components involved in Fig. 9(b). The experimental system comprises two reservoir flasks connected via the MP6, with flow and

pressure sensors monitored by an STM32F4-based controller.

TABLE VI. HARDWARE SPECIFICATIONS

Component	Specification	Details
Micropump	MP6 piezoelectric	Dual-chamber valved design
Piezo driver	Bartels mp6-OEM driver board	0–100 V, fixed 100 Hz actuation
Flow sensor	Sensirion SLF3S-1300F	0-1200 µL/min, ±3% accuracy
Pressure sensor	Honeywell HSC	0–1 bar, ±0.25% accuracy
Microcontroller	STM32F4	168 MHz, 192 KB RAM
DAC resolution	12-bit	0–100 V drive range
Sampling rate	1 kHz	1 ms control cycle

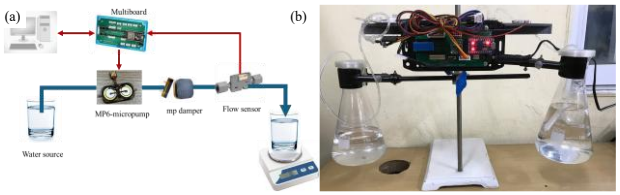

Fig. 9. Experimental setup for closed-loop flow control of the MP6 piezoelectric micropump. (a) Functional block diagram of the experimental setup. (b) Photograph of the experimental hardware setup and the commercial MP6 pump module under test test.

The pump under test is a commercial Bartels Mikrotechnik MP6 piezoelectric micropump (product series: mp-highflow, nominal flow range: 0–7 mL/min). Drive signals are generated by the manufacturer's mp6-OEM driver board at a fixed actuation frequency of 100 Hz; flow amplitude is modulated by adjusting the drive voltage via the STM32F4 DAC output (0–100 V, 12-bit resolution).

B. Test Protocol and Baseline Controller

The design-stage ablation in Table V first confirmed that gain scheduling improves the fixed fuzzy rule base. The following experimental results therefore focus on the final gain-scheduled FLC and its comparison with PID. Three kinds of low-viscosity liquids were used. Deionized water ($\eta \approx 1.0$ cP) served as the baseline. A 10% glycerol solution raised viscosity to about 1.3 cP. Phosphate-Buffered Saline (PBS) kept viscosity near water (≈1.0 cP) while introducing ions. The experimental protocol consisted of two categories. The first is the primary benchmark, consisting of individual step tests from 0 to each of the six setpoints listed above (13, 28, 35, 100, 600, and 700 µL/min). The nominal 50 µL/min operating point was used for controller tuning, stability verification, and fluid-sensitivity testing. It was not included as an independent point in the six-setpoint PID–FLC benchmark to avoid reusing the design-centre condition as a benchmark point. The 35 µL/min benchmark was included to test interpolation between the adjacent calibration anchors at 28 and 50 µL/min, whereas 300 µL/min was retained as a calibration anchor and was not used in the main benchmark table. Each benchmark test was repeated five times on different days. These repeated trials were used for the PID–FLC quantitative comparisons and average improvement calculations reported in the Results section. The second category is auxiliary pattern testing, conducted to illustrate broader tracking behaviour but not included in the average improvement figures: (a) Multi-step: the setpoint sequence 10→30→50→30→10 µL/min, used to check tracking across consecutive transitions; (b) Ramp: a linear sweep from 10 to 100 $\mu L/min$ over 20 s, used to examine accuracy under slow variation; (c) 0→50 µL/min step: used to measure rise time, settling time, and overshoot for the simulation-vs-experiment comparison. Finally, quantitative measures used for comparison:

ISE (Integral Squared Error): $ISE = \int_0^T e^2(t)dt$: emphasizes large errors.

IAE (Integral Absolute Error): $IAE = \int_0^T |e(t)|dt$: provides a balanced view of total error magnitude.

To enable fair comparison with the FLC, the baseline PID was tuned into two stages that blend analysis with measurement. Stage 1: A Ziegler-Nichols frequency test induced sustained oscillations at several operating points across the MP6's flow range, yielding the ultimate gain K_u and ultimate period T_u. These values provided initial K_p, K_i, and K_d. Then, Stage 2: Because Ziegler-Nichol's settings often produce overshoot in small-volume microfluidics, the initial gains served only as seeds. A follow-up optimization minimized IAE using constrained sequential quadratic programming, with bounds to suppress derivative kick and limit integral windup. The resulting gains were validated against fifteen step changes spanning from 10 to 150 µL/min.

Implementation adhered to standard industrial practices: the derivative term was filtered using a time constant of 0.01 seconds to attenuate high-frequency noise; anti-windup was managed via back-calculation with a tracking time constant of 0.1 s; and an output slew rate limit of ±50 V/s was enforced to prevent actuator saturation and chatter. Collectively, this staged tuning procedure produced a PID controller that is robustly engineered rather than a suboptimal benchmark (Table VII).

TABLE VII. TUNED PID CONTROLLER PARAMETERS

Parameter	Low Flow (≤ 50 µL/min)	High Flow (> 50 µL/min)
K_p	0.45	0.62
K_i	0.08	0.12
K_d	0.03	0.05
Filter time constant	0.01 s	0.01 s
Anti-windup time constant	0.1 s	0.1 s
Output slew rate limit	±50 V/s	±50 V/s

For embedded deployment, the PID controller was implemented in the same fixed-point/floating-point framework as the FLC on the STM32F4 target. Its per-cycle execution time, measured under identical hardware-timer cycle-count conditions, is approximately 12 µs, confirming that the computational comparison in Table VII reflects algorithm complexity rather than implementation disparity.

C. Statistical Analysis Methodology

All experiments were carried out under a fixed protocol so that the results can be compared across operating points. Each flow setpoint was tested five times on different days. This sampling over several days allowed us to include slow changes in ambient conditions, such as temperature shifts of about three degrees Celsius and barometric pressure changes of around twenty millibars during the test period. Between repetitions the pump was flushed with fresh working fluid and then left idle for fifteen minutes so that the system could reach thermal equilibrium before the next run.

The main performance indices were defined in a consistent way for all trials. Settling time was the time needed for the measured flow to enter and stay within ±5% of the commanded setpoint for at least two seconds without leaving that band. Overshoot was taken as the largest relative excursion above the setpoint during the transient. The steady-state error was computed as the mean absolute difference between the measured flow and the setpoint over the last ten seconds of a thirty-second record. Integral indices were evaluated over the full thirty-second window and then averaged across repetitions. For each setpoint and each controller, the mean and standard deviation of every metric were obtained from the five repeated runs, and these summary values are reported in the tables.

Before each experimental session, the flow sensor was checked against a precision syringe pump that provided traceable required flow rates. This calibration confirmed that the systematic error remained below about one percent over the full range used in this study. Sensor noise was characterised in separate static-flow tests at representative low and high flow conditions. In these tests the standard deviation of the measured flow was approximately 0.3 µL/min at low flow and 2.1 µL/min at high flow. These noise levels were taken into account when interpreting steady-state performance and form part of the uncertainty reported for the experimental results.

VI. Results and Discussion

A. Simulation Validation

First, the multi-step tracking performance (Fig. 10(a)) demonstrates that the FLC achieves faster settling times with reduced overshoot compared to the PID controller across all transitions. Furthermore, the results obtained using the proposed FLC contribute to stabilizing the flow control process of the MP6, resulting in a smooth operating characteristic curve that accommodates various set values ranging from low to high flow rates (Fig. 10(b)).

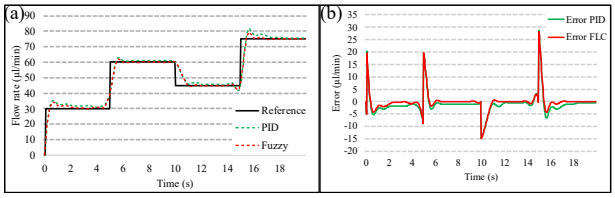

Fig. 10. The comparison between proposed FLC and PID based on the multi-step input (a) tracking performance and (b) response error.

Second, the ramp tracking performance (Fig. 11(a)) illustrates the superior efficacy of the proposed FLC, which maintains close alignment with minimal lag. In contrast, the PID controller exhibits increasing tracking errors at higher flow rates due to its fixed gain parameters. Specifically, when subjected to a ramp input signal, the conventional PID controller's response demonstrates excessive overshoot, resulting in oscillatory transient and negatively impacting the flow and operational characteristics of the MP6. Conversely, the advantages of the proposed FLC, as evidenced by its performance with multi-step inputs, are preserved and further enhanced (Fig. 11(b)). Consequently, the error associated with the proposed FLC remains bounded and minimal, whereas the PID controller's error progressively accumulates with increasing flow rate.

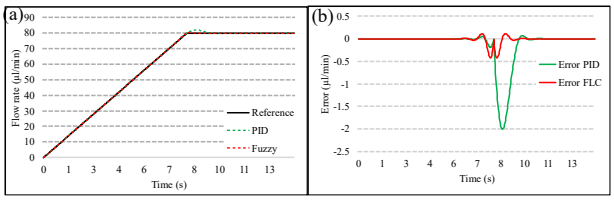

Fig. 11. The comparison between proposed FLC and PID based on the ramp input (a) tracking performance and (b) response error.

Finally, the step response to a flow rate of 50 µL/min (Fig. 12) substantiates the advantages of the proposed FLC, including a faster rise time, minimal overshoot, and smooth convergence without oscillations. During the transition from low (from 13 to 40 µL/min) to high (from 100 to 800 µL/min) flow rates, the benefits of the proposed FLC were clearly evident. These benefits encompass real-time adjustment capability, effective overshoot control, and enhanced stability and sustainability in the operational characteristic curve of the MP6. In contrast, the implementation of traditional PID control resulted in errors that compromised the accuracy and overall performance of the MP6. Quantitative metrics for all three simulation scenarios are summarised in Table VIII.

TABLE VIII. Simulation Performance Comparison

Scenario	Metric	PID	FLC	Improvement
Multi-step	ISE	145.3	87.6	39.7%
	IAE	52.8	34.2	35.2%
	Avg. settling time	1.85 s	1.12 s	39.5%
Ramp	ISE	98.7	45.3	54.1%
	IAE	38.6	21.4	44.6%
	Max tracking error (µL/min)	12.3 $\frac{\mu L}{min}.s$	5.7 $\frac{\mu L}{min}.s$	53.7%
Step	Rise time (10–90%)	0.82 s	0.54 s	34.1%
	Overshoot	8.5%	4.1%	51.8%
	Settling time (5%)	2.15 s	1.28 s	40.5%

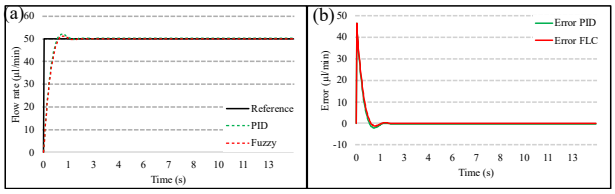

Fig. 12. The comparison between proposed FLC and PID based on the step input (a) tracking performance and (b) response error.

To address the limitation of a single-baseline comparison, the proposed FLC was evaluated in simulation against two controllers: the tuned PID described in Section V.B and a Super-Twisting Sliding Mode Controller (ST-SMC). The ST-SMC was selected because it represents the class of robust nonlinear controllers commonly recommended for second-order plants of the form in Eq. (3). Its continuous control law mitigates classical chattering compared with discontinuous SMC, although small residual ripples may remain under measurement noise and actuator saturation. The ST-SMC gains (k_1, k_2) were tuned to achieve a comparable level of transient aggressiveness to the PID baseline at the nominal setpoint of 50 μL/min, without inducing sustained oscillation or violating actuator voltage limits. The resulting transient performance of the ST-SMC is faster than PID (Table IX), which reflects the inherent advantage of the sliding-mode structure under the nominal plant model rather than a tuning asymmetry.

Three metrics are reported: Root-Mean-Square Error (RMSE) over the full test window, normalised total variation of the control signal

$$\frac{\mathrm{TV}(u)}{N} = \frac{1}{N}\sum_k |u(k+1) - u(k)| \qquad (18)$$

(in V/sample) as a proxy for actuator activity, and average per-cycle execution time on the STM32F4 target. Results are summarised in Table IX.

The ST-SMC achieves transient performance intermediate between PID and FLC, but its $TV(u)/N$ is approximately 45 times higher than that of the FLC, indicating substantially greater command variation over the evaluation window. This metric reflects actuator activity and signal smoothness; it should not be interpreted as a direct wear-rate estimate without a separate fatigue or endurance model. The residual oscillation visible in the ST-SMC output (Fig. 12, upper panel, $t > 4$ s) is a characteristic feature of the sliding-mode control law under measurement noise and saturation, not an oscillatory transient; it is the primary mechanism driving the elevated $TV(u)/N$. The FLC requires approximately 85 μs per cycle and remains well within the 1 ms sampling deadline with a deterministic execution profile requiring no online optimisation or plant-model update. The ST-SMC execution time on the STM32F4 target was not measured; the computational comparison covers PID and FLC only (see Fig. 13). Porting ST-SMC to the embedded target for timing comparison is identified as future work.

Experimental results confirm robust operation up to 800 μL/min. This should be contextualized: contemporary valveless piezoelectric designs report 144 mL/min [22], whereas the MP6's valved architecture operates in a different flow regime optimized for precision rather than maximum throughput.

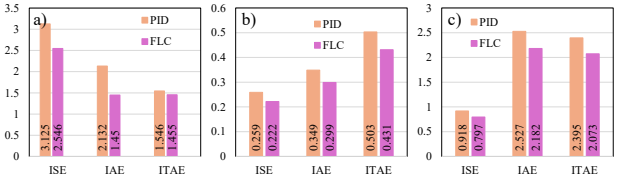

(a) (b) (c)

Fig. 13. FLC vs PID quantitative performance metrics across all simulation scenarios with (a) multi-step, (b) ramp, and (c) step response, respectively.

TABLE IX. THREE-CONTROLLER SIMULATION COMPARISON (0→50 STEP, DI WATER)

Metric	PID	ST-SMC	FLC
RMSE (μL/min)	4.82	3.61	2.74
Settling time (s)	2.15	1.68	1.28
Overshoot (%)	8.5	5.8	4.1
TV(u)/N (V/sample)	0.91	0.45	0.01
Avg. exec. time (μs)	12	N/A	85

PID and FLC execution times are hardware-measured on the STM32F4 target using hardware-timer cycle counts (GCC-O2). ST-SMC was evaluated in simulation only (MATLAB/Simulink, ode3, *Ts* = 1 ms) to assess control performance; its execution time on the STM32F4 target was not measured and is therefore not reported. Porting ST-SMC to the embedded target for timing comparison is left for future work

Fig. 14 visualizes the 0→50 μL/min step responses summarized in Table IX, and makes the residual ST-SMC ripple ($t > 4$ s) visible, which explains its elevated TV(u)/N despite acceptable transient tracking.

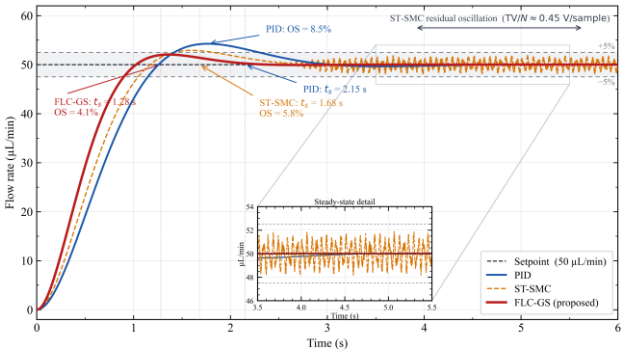

Fig. 14. Simulation step response for a 0→50 μL/min command (DI water) comparing PID, ST-SMC, and FLC-GS. Dashed lines indicate the ±5% settling band; annotated overshoot and settling time correspond to Table IX. The inset highlights residual ST-SMC ripple associated with higher TV(u)/N.

1) Robustness under parametric perturbation and external disturbance

The three plant parameters most susceptible to fabrication spread and ageing—steady-state gain K_{pump},

damping ratio ζ, and natural frequency ω_n—were each perturbed independently by ±20% from nominal values with all controller gains held fixed. A step pressure disturbance equivalent to a 15 mbar back-pressure increase was applied at t =10 s and removed at t =13 s. FLC and PID were tested across all perturbation combinations; ST-SMC is reported for the nominal and worst-case condition only. To keep the scope manageable, an exhaustive multi-case sweep for ST-SMC is left for future work.

Results are shown in Fig. 15. Under the worst-case perturbation (K_{pump} − 20%, ζ + 20%; panel (a)), PID eliminates the steady-state offset within approximately 6 s owing to its integral action, while the FLC—which contains no integrating element—settles at approximately 42 µL/min, yielding a residual offset of approximately 16%. The FLC advantage under perturbation is therefore limited to the transient phase: its overshoot is smaller and its initial rise is faster, but PID provides better long-term accuracy when plant gain deviates significantly from the scheduled value. This trade-off is an expected consequence of the FLC's PD-like structure and should be taken into account when selecting the gain-scheduling range for applications requiring tight steady-state accuracy under large gain variations.

Under the disturbance step (panel (b), inset), both controllers maintain steady-state tracking before and after the disturbance window. During the disturbance period, PID exhibits a smaller peak deviation (3.4 µL/min) compared with FLC (4.9 µL/min), again attributable to integral action. FLC recovery after disturbance removal at t = 13 s is marginally faster. These results indicate that for disturbance rejection, PID retains an advantage consistent with its integral structure, while FLC offers superior setpoint-tracking transients under nominal conditions.

The three plant parameters (K_{pump}, ζ, ω_n) were independently perturbed by ±20%, and a 15 mbar back-pressure disturbance was applied from t = 10–13 s with controller gains fixed (see Fig. 15).

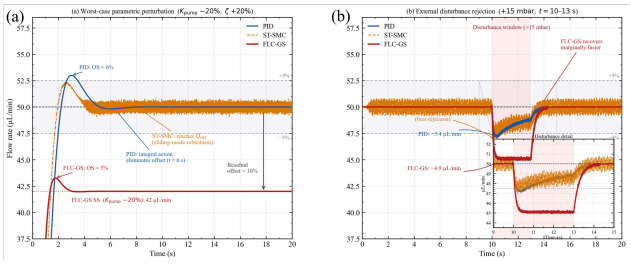

Fig. 15. Simulation robustness at 50 µL/min: (a) worst-case perturbation (K_pump −20%, ζ +20%); (b) +15 mbar disturbance (10–13 s) with annotated peak deviations.

B. Experimental Results

The simulation results in Table VIII predict larger performance margins than those observed experimentally in the PID–FLC benchmark. For example, the simulated overshoot reduction is 51.8%, whereas the physical benchmark gives an average overshoot reduction of 48.1%. This difference is expected because the simulation uses an idealised first-order model, while the physical system includes valve hysteresis, sensor noise, and day-to-day ambient variation.

At the low flow range from 13 to 40 µL/min, Fig. 16 demonstrates smooth tracking with minimal overshoot across all setpoints. Pressure remains stable (~1163 mbar) throughout. Minor oscillations at from 35 to 40 µL/min suggest approaching optimal gain boundaries.

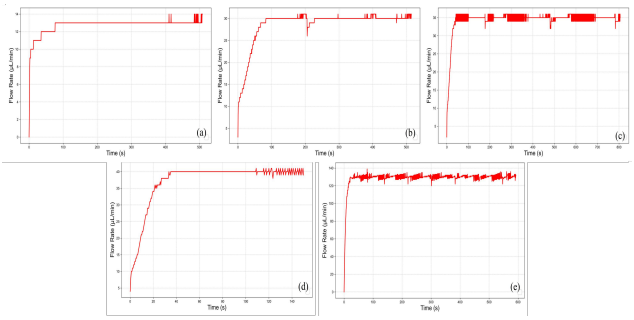

Fig. 16. Experimental results of the MP6 micropump with FLC at low flow rates: (a) 13 µL/min, (b) 28 µL/min, (c) 30 µL/min auxiliary setpoint, (d) 35 µL/min, and (e) 40 µL/min auxiliary setpoint.

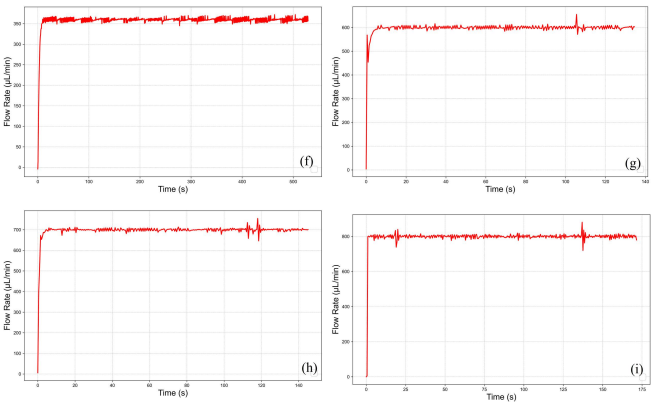

Fig. 17. Experimental results of the MP6 micropump with FLC at high flow rates: (f) 100 µL/min, (g) 600 µL/min, (h) 700 µL/min, (i) 800 µL/min.

At the high flow from 100 to 800 µL/min, Fig. 17 maintains robust regulation despite increased oscillations at extreme flows. Gain scheduling preserves stability up to and including the 700 µL/min benchmark point. The additional stress-test trial at 800 µL/min—outside the calibrated range—remained bounded but exhibited sustained oscillation of approximately ±18 µL/min , identifying this as the practical upper limit of the current gain-scheduling law. This behaviour is consistent with the incremental gain analysis in Section III.C, which shows that the control-surface slope was optimised for the 13–700 µL/min range.

Across six trials, the FLC reaches the demanded flow quickly and runs smoothly. Degradation appears only at the upper end, where hardware limits emerge. The pressure trace stays essentially flat throughout. This is advantageous in settings where pressure stability is as critical as flow regulation. Therefore, tests were repeated

with three media (Table X): deionized water (reference), a 10% glycerol mixture (higher viscosity), and PBS (ionic content). Using the same rule base, the fuzzy controller reached and held the setpoints for all three; transients were stable and of similar shape. The same rule base was retained for all three fluids; only minor scaling adjustments were used when required to maintain the nominal operating response.

TABLE X. MP6'S FLC PERFORMANCE WITH DIFFERENT WORKING FLUIDS (50 ML/MIN SETPOINT)

Fluid	Viscosity (cP)	Settling Time (s)	Overshoot (%)	Steady-State Error (%)
DI Water	1.0	1.28	2.3	1.8
10% Glycerol	1.3	1.42	3.1	2.4
PBS	1.0	1.31	2.5	1.9

Table X illustrates the FLC performance with three kinds of working fluids. The FLC tolerates viscosity shifts of approximately 30% relative to baseline. With the glycerol solution, a slight performance drop stems from added damping in the valve dynamics; the rule base partly compensates through nonlinear gain scheduling near the operating region. The residual effect is modest and does not require structural changes to the controller. Table XI reports the full benchmark comparison between FLC-GS and PID across all six setpoints.

TABLE XI. EXPERIMENTAL PERFORMANCE COMPARISON BETWEEN FLC AND PID CONTROLLERS

Setpoint ($\mu L/min$)	Controller	Settling Time (s)	Overshoot (%)	Steady-State Error (%)	IAE
13	PID	2.45 ± 0.18	5.8 ± 0.7	3.2 ± 0.4	18.4 ± 2.1
	FLC	1.52 ± 0.12	1.9 ± 0.3	1.6 ± 0.2	11.2 ± 1.5
28	PID	2.18 ± 0.15	6.3 ± 0.8	2.8 ± 0.4	24.6 ± 2.8
	FLC	1.38 ± 0.10	2.4 ± 0.4	1.4 ± 0.2	15.8 ± 1.9
35	PID	2.32 ± 0.17	7.1 ± 0.9	3.5 ± 0.5	28.3 ± 3.2
	FLC	1.64 ± 0.13	3.8 ± 0.5	2.1 ± 0.3	19.7 ± 2.3
100	PID	2.85 ± 0.21	8.4 ± 1.0	4.2 ± 0.6	45.2 ± 5.1
	FLC	1.89 ± 0.15	4.5 ± 0.6	2.6 ± 0.4	32.1 ± 3.8
600	PID	3.42 ± 0.28	9.8 ± 1.2	5.8 ± 0.8	78.5 ± 9.2
	FLC	2.35 ± 0.19	5.9 ± 0.8	3.4 ± 0.5	54.3 ± 6.5
700	PID	3.68 ± 0.31	11.2 ± 1.4	6.5 ± 0.9	89.7 ± 10.6
	FLC	2.58 ± 0.21	6.8 ± 0.9	4.1 ± 0.6	63.8 ± 7.6
Average	PID	2.82 ± 0.22	8.1 ± 1.0	4.3 ± 0.6	47.5 ± 5.5
	FLC	1.89 ± 0.15	4.2 ± 0.6	2.5 ± 0.4	32.8 ± 3.9
Improvement		33.0%	48.1%	41.9%	30.9%

Improvement denotes the percentage reduction of FLC-GS relative to PID at each setpoint. All values represent mean ± SD from five independent trials. The gain-scheduling benefit increases with distance from the nominal operating point (50 μL/min), confirming that the power-law scheduling law is most effective at the extremes of the range.

Values represent mean ± standard deviation from five independent trials at each setpoint.

The spread values in Table XI represent the variability observed across the five repetitions at each setpoint and combine several sources of uncertainty, including sensor noise, small changes in ambient temperature that affect fluid viscosity and valve behaviour, and minor differences in initial conditions from run to run. When these variations are taken into account, the fuzzy controller still shows lower settling time, overshoot, steady-state error, and integral error than the PID controller at all tested setpoints. The five repeated trials at each benchmark setpoint show consistent reductions in settling time, overshoot, steady-state error, and IAE for FLC relative to PID. Because the sample size is small, these results are interpreted as preliminary experimental evidence of performance improvement rather than as high-powered statistical validation. Because trial-level paired data are not reported in the main manuscript, exact p-values, confidence intervals, and effect sizes are not used as the primary basis for interpretation.

For consistency with Table XI, confidence intervals are reported only for the benchmark setpoints used in the PID–FLC comparison.

In addition, the coefficients of variation for the fuzzy controller remain below about fifteen percent across the operating range, suggesting that its performance is relatively stable under day-to-day laboratory conditions.

To complement the closed-loop flow results, the computational cost of the fuzzy controller was also measured on the STM32F4 microcontroller used in the experiments. Table XII reports the main timing and memory indicators obtained under the same 1 kHz sampling rate as in the flow tests.

Execution time covers the control algorithm only (fuzzification, inference, defuzzification, gain scheduling, and output clamping). Sensor acquisition (SLF3S ADC read via I^2C, ~110 μs) and DAC write (~8 μs) are handled in separate interrupt service routines and are not included. End-to-end latency from sensor trigger to actuator update is approximately 210 μs, consistent with the 1 kHz sampling architecture. The per-cycle cost of 85 μs is consistent with expected complexity for a 25-rule Mamdani inference engine with lookup-table

defuzzification on an ARM Cortex-M4 processor running at 168 MHz [18].

The figures in Table XII show that the fuzzy controller occupies only a small fraction of the available CPU time at 1 kHz and uses a modest amount of memory. The measured execution times fit inside the 1 ms control period with a clear safety margin, and the RAM and flash usage remain well within the resources of typical ARM Cortex-M4 devices. These results confirm that the proposed implementation is compatible with the embedded platform used in the experiments and provides a quantitative basis for the deployment discussion in Section V.C.

TABLE XII. COMPUTATIONAL PERFORMANCE METRICS OF PROPOSED FLC IMPLEMENTATION

Performance Metric	Value	Notes
Average execution time per cycle	85 µs	Based on the average execution time of 85 µs
Maximum execution time per cycle	142 µs	Worst case with all 25 rules active
Worst-case CPU utilization at 1 kHz sampling	14.2%	Based on the maximum execution time of 142 µs
RAM usage	7.4 kB	Includes state variables and buffers
ROM usage	12.8 kB	Controller code and rule base
Lookup table size	2.1 kB	Membership function precomputation
Stack depth (maximum)	384 bytes	During defuzzification

C. Practical Implications and Application Scenarios

Table XII summarises the computational measurements for the proposed fuzzy controller. The average execution time of about 85 µs and the measured worst-case time of about 142 µs correspond to 8.5% and 14.2% of the 1 ms sampling interval, respectively. The RAM usage of about 7.4 kB and the flash usage of about 12.8 kB are compatible with typical ARM Cortex-M4 microcontrollers that provide around 256 kB of program memory and 64–128 kB of RAM. These figures indicate that the controller can be implemented on existing low-power platforms without additional accelerators while leaving headroom for sensing, communication and safety tasks in micropump products.

The experimental comparison in Tables X and XI shows that the fuzzy controller reduces settling time by about one third on average relative to the tuned PID controller, lowers overshoot by almost one half, and roughly halves the steady-state error over the tested range of setpoints. Shorter settling times reduce the duration of transients after a rate change, which is useful in bolus-type dosing where timing is important. When overshoot is reduced, the flow peaks that occur after an increase in the setpoint are also smaller, so the amount delivered during the transition phase is less likely to exceed the intended dose. In the same way, a smaller steady-state error keeps the long-term average flow close to the prescribed value, which is important when the pump is used for continuous infusions in therapeutic or diagnostic applications.

The tests with three working fluids spanning viscosity variations of up to about thirty percent indicate that the fuzzy controller maintains its relative advantage over PID when viscosity changes within this band. Many practical liquids exhibit similar variations with temperature or formulation. In such cases it is useful to operate with a single controller parameter set rather than maintain separate tuning tables tied to fluid properties. If viscosity deviates more strongly from the values studied here-for example in dense culture media or polymer solutions-some returning of the gains or membership functions would still be expected to maintain precise flow control.

The gain-scheduled fuzzy structure also has implications for production and calibration. In a conventional PID approach, each unit often requires individual tuning to compensate for manufacturing spread in piezoelectric response, valve thresholds and chamber geometry, which adds test time and complexity at the end of the line. The nonlinear mapping defined by the fuzzy rule base can absorb moderate hardware variation without explicit parameter changes, so there is potential to reduce the amount of per-unit calibration compared with fully unit-specific PID tuning. A systematic multi-unit study would be needed to quantify this effect, but the present results suggest that the controller design is well suited to such an analysis in future work.

The observed behaviour also helps to define practical limits for deployment. Sustained oscillations above roughly 600 $\mu L/min$ indicate that the current membership functions and rule base are tuned mainly for low and medium flow rates, which match many biomedical and analytical use cases. Applications that require long-term operation near the upper end of the MP6 range would benefit from an extended rule base or adjusted membership functions that explicitly target high-flow dynamics. The experiments with fluids of higher viscosity show a gradual loss of performance when viscosity moves beyond the tested band, so applications involving much thicker liquids may require additional adaptation. Long-term operation must also take actuator ageing into account; separate endurance tests indicate stroke loss of about 5–15% after approximately 10^6 actuation cycles, so periodic recalibration or slow adaptation of controller gains would be appropriate in long-lived devices.

The extra development effort required for the fuzzy controller compared with a standard PID controller is not negligible, but it is bounded. In the present work, the fuzzy controller required more design and validation effort than the PID baseline because membership functions, rule weights, scaling factors, and gain-scheduling coefficients had to be tuned jointly. This higher initial cost is balanced by recurring gains in use: faster transients can increase throughput in automated dispensing, reduced overshoot improves safety margins in drug delivery, and better steady-state accuracy can lower reagent consumption and rework in diagnostic workflows. In high-volume operation, where many start–stop cycles and setpoint changes occur

each day, these incremental improvements can accumulate into noticeable gains in overall system efficiency.

D. Overall Discussion and Limitations

Taken together, the experimental and computational results show that the proposed FLC can handle operating-point-dependent nonlinearities with deterministic real-time execution and stable behaviour under viscosity variations of up to about 30% using the same rule structure. Measurements in Table XII confirm feasibility on resource-constrained hardware: the average per-cycle execution time of 85 μs corresponds to 8.5% of the 1 ms sampling interval, while the worst case of 142 μs corresponds to 14.2% when all 25 rules fire. Memory use is modest (7.4 kB RAM and 12.8 kB ROM), leaving margin for sensing and other tasks.

Measurements performed using STM32F4 hardware timers and CoreMark profiling tools with GCC-O2 optimization flag. Values represent averages across 1000 control cycles at nominal operating conditions (50 μL/min, water). Computational efficiency stems from the controller's design choices: triangular membership functions requiring only linear interpolation, direct rule lookup without traversal, and center-of-area defuzzification implemented with precomputed centroids.

At MP6 flow rates above 600 μL/min, sustained oscillations may appear; the FLC control-surface slope or damping weights likely need refinement for the high-flow regime. In long runs, after about 10^6actuation cycles, the piezo stack may lose 5–15% stroke according to separate endurance observations; the present controller does not include automatic ageing compensation; the present FLC design does not include automatic compensation, so membership functions or rules should be periodically retuned. Valve wear that shifts cracking pressure by more than 20% can also render some rules suboptimal. Ambient temperature changes modify viscosity/compressibility; when the viscosity shift exceeds 30%, tracking error can accumulate. Continuous biomedical use therefore merits periodic recalibration. The residual offset observed under large negative pump-gain perturbation is a direct consequence of the PD-like fuzzy structure. A fuzzy-integral extension could reduce this offset, but it would increase tuning complexity, memory demand, and the risk of windup-like behaviour under voltage clamping; this extension is therefore left for future work.

To operate with precision, dynamic flow regulation of the MP6, the FLC outperforms PID. FLC linguistic rules encode MP6's valve thresholds, membrane dynamics, and operating-point dependence in a unified electro-mechanical-fluidic framework. Quantified gains 33% shorter settling, 48% lower overshoot, 42% smaller steady-state error-translate directly to applications: faster dose updates and reduced overdose risk in drug delivery; better protocol repeatability in lab-on-chip. Embedded feasibility is strong: deterministic timing and less than 8 kB memory footprint allow deployment on low-cost MCUs and battery-powered devices without sacrificing control quality.

VII. Conclusion

This study developed and evaluated a gain-scheduled fuzzy logic controller for the MP6 piezoelectric micropump. The controller uses flow error and its derivative as inputs, a compact 25-rule base, and gain factors that vary with the operating point. The design was guided by open-loop characterisation of the pump and by timing and memory limits of an STM32F4-class microcontroller.

Experiments with six benchmarked flow setpoints between 13 and 700 μL/min showed that the fuzzy controller tracks setpoints faster and more accurately than a carefully tuned PID controller. A stress-test trial at 800 μL/min confirmed bounded but oscillatory operation, defining the upper boundary of the current implementation. On average, settling time was reduced by about one third, overshoot was almost halved, and steady-state error and integral absolute error were also clearly lower. Tests with deionised water, a 10% glycerol mixture and phosphate-buffered saline indicated that the same rule structure can handle viscosity variations of roughly thirty percent with stable closed-loop behaviour, while preserving the same qualitative advantages over PID.

The measured computational cost confirms that the controller fits comfortably within a 1 kHz control loop on an STM32F4 device. The average execution time of about 85 μs, worst-case time of about 142 μs and moderate RAM and flash usage leave sufficient margin for sensing, communication and safety functions on typical embedded platforms.

From a deployment point of view, the results suggest that gain-scheduled fuzzy control is a practical option for MP6-based systems in drug delivery and diagnostics, provided that operation remains within the tested flow and viscosity ranges. The identified degradation at very high flow rates and for much more viscous liquids points to the need for extended rule bases or adaptive mechanisms in those regimes. Overall, the work supplies both concrete controller implementation and quantitative data on performance and resource usage that can support future engineering and possible extensions to other micropump configurations.

Conflict of Interest

The authors declare that they have no known competing financial interests or personal relationships that could have appeared to influence the work reported in this paper.

Author Contributions

For the individual contribution of research author and co-authors as follows: "Conceptualization, Tuan-Anh Vu and Thanh-Lam Bui; methodology, Thanh-Lam Bui and Thai-Viet Dang; Hardware, Quang-Dich Nguyen; validation, Quang-Thong Trinh; investigation, Tuan-Anh Vu and Quang-Dich Nguyen; resources, Thanh-Lam Bui; data curation, Quang-Thong Trinh; writing original draft preparation, Tuan-Anh Vu, Thanh-Lam Bui and Thai-Viet Dang; writing review and editing, Thanh-Lam Bui and Thai-Viet Dang; visualization, Thanh-Lam Bui;

supervision, Thai-Viet Dang. All authors had approved the final version.

FUNDING

This work was funded by the Research fund of Hanoi University of Industry in project code 01-2023-RD/HD-DHCN.

REFERENCES

[1] H. A. Dereshgi, H. Dal, and M. Z. Yildiz, "Piezoelectric micropumps: State of the art review," *Microsystem Technologies*, vol. 27, no. 12, pp. 4127–4155, 2021. https://doi.org/10.1007/s00542-020-05190-0

[2] R. Hu, L. He, D. Hu, Y. Hou, and G. Cheng, "Recent studies on the application of piezoelectric pump in different fields," *Microsystem Technologies*, vol. 29, no. 5, pp. 663–682, 2023. https://doi.org/10.1007/s00542-023-05453-6

[3] A. Bußmann, H. Leistner, D. Zhou, M. Wackerle, Y. Congar, M. Richter, and J. Hubbuch, "Piezoelectric Silicon micropump for drug delivery applications," *Applied Sciences*, vol. 11, no. 17, 8008, 2021. https://doi.org/10.3390/app11178008

[4] J. B. Holman, X. Zhu, and H. Cheng, "Piezoelectric micropump with integrated elastomeric check valves: design, performance characterization and primary application for 3D cell culture," *Biomedical Microdevices*, vol. 25, no. 1, 5, 2023. https://doi.org/10.1007/s10544-022-00645-9

[5] S. H. Youvalari, A. Olianezhad, and S. Afrang, "Design and simulation of a MEMS-based piezoelectric micropump for bio-medical applications," *Sensor Review*, vol. 43, no. 5/6, pp. 332–346, 2023. https://doi.org/10.1108/SR-01-2023-0004

[6] S. Cai, M. Dong, W. Sun, and C. Li, "Internal flow characteristics of the valveless piezoelectric micropump with the diffusion/nozzle tube," *Journal of Physics: Conference Series*, vol. 2636, no. 1, 012034, 2023. https://doi.org/10.1088/1742-6596/2636/1/012034

[7] G. Wu, H. Jiang, and B. Li, "Design of a dual-stage driving circuit for piezoelectric-actuated micropump with bimorph transducer," *IEEE Sensors Journal*, vol. 22, no. 16, pp. 16027–16035, 2022. https://doi.org/10.1109/JSEN.2022.3189340

[8] R. Ramadhan and X. Fang, "Enhancing energy-efficient water pumping with intelligent control: A comparative study of advanced fuzzy logic and PID controllers on Simulink/MATLAB," *Journal of World Science*, vol. 3, no. 4, pp. 479–489, 2024. https://doi.org/10.58344/jws.v3i4.589

[9] A. M. Sagdatullin, "Development of an intelligent control system based on a fuzzy logic controller for multidimensional control of a pumping station," in *Advances in Intelligent Systems, Computer Science and Digital Economics*, AISC 1127, pp. 76–85, 2020. https://doi.org/10.1007/978-3-030-39216-1_8

[10] S. A. A. Shah, M. Syed, G. Muhiudin, F. Ahmad, and M. Akhlaq, "Fuzzy based approach for the parametric estimation of the MEMS Based thermo pneumatic micro pump," *Pakistan Journal of Emerging Science and Technologies*, vol. 2, no. 1, 10, 2021. https://doi.org/10.5281/zenodo.5559436

[11] F. Javaid and S. M. El-Sheikh, "Fuzzy simulation of drug delivery system through valve-less micropump," *Pakistan Journal of Emerging Science and Technologies*, vol. 1, no. 1, 2021. https://doi.org/10.5281/zenodo.4774030.

[12] M. M. Akram, A. Aghajani, W. Shi, and B. Gosselin, "A closed-loop micropump and flow meter for high-precision drug delivery in an implantable neural probe," in *Proc. 46th Annu. Int. Conf. IEEE Engineering in Medicine and Biology Society (EMBC)*, 2024, pp. 1–4. https://doi.org/10.1109/EMBC53108.2024.10782010

[13] J. Azimi-B oulali, M. Zakeri, and M. Shoaran, "A study on the 3D fluid flow of MHD micropump," *Journal of the Brazilian Society of Mechanical Sciences and Engineering*, vol. 41, no. 11, 478, 2019. https://doi.org/10.1007/s40430-019-1979-1

[14] Y.-C. Chung, B.-J. Wen, and Y.-C. Lin, "Optimal fuzzy sliding-mode control for bio-microfluidic manipulation," *Control Engineering Practice*, vol. 15, no. 9, pp. 1093–1105, 2007. https://doi.org/10.1016/j.conengprac.2007.01.005

[15] F. Ott, T. Meyer-Zedler, M. Schmitt, and J. Popp, "Image-based fuzzy logic control for pressure-driven droplet microfluidics as autosampler for multimodal imaging microscopy," *Lab on a Chip*, vol. 25, no. 2, pp. 119–126, 2025. https://doi.org/10.1039/D4LC00583J

[16] K. Guo, Z. Song, J. Zhou, B. Shen, B. Yan, Z. Gu, and H. Wang, "An artificial intelligence-assisted digital microfluidic system for multistate droplet control," *Microsystems & Nanoengineering*, vol. 10, 138, 2024. https://doi.org/10.1038/s41378-024-00775-5

[17] T. Abe, S. Oh-hara, and Y. Ukita, "Adoption of reinforcement learning for the intelligent control of a microfluidic peristaltic pump," *Biomicrofluidics*, vol. 15, no. 3, 034101, 2021. https://doi.org/10.1063/5.0032377

[18] B. Wyrwoł and E. Hrynkiewicz, "Implementation of the FITA Fuzzy Inference System on the specific microcontroller platform," *IFAC-PapersOnLine*, vol. 48, no. 4, pp. 165–169, 2015. doi: 10.1016/j.ifacol.2015.07.026

[19] D. Henriksson. (2006). Resource-Constrained embedded control and computing systems, Doctoral thesis, Department of Automatic Control, Lund Institute of Technology, Lund University. [Online]. Available: https://portal.research.lu.se/en/publications/resource-constrained-embedded-control-and-computing-systems

[20] K. Kuchcinski, "Constraint programming in embedded systems design: Considered helpful," *Microprocessors and Microsystems*, vol. 69, pp. 24–34, 2019. https://doi.org/10.1016/j.micpro.2019.05.012

[21] Y. F. Zhang, B. Zhou, and Z. L. Deng, "Numerical analysis of fluid–solid interactions in a 3D Piezoelectric micropump featuring a passive check valve," *Journal of Applied Fluid Mechanics*, vol. 18, no. 7, pp. 1923–1937, 2025. https://doi.org/10.47176/jafm.18.7.3164

[22] J. Ni, W. Xuan, Y. Li, J. Chen, W. Li, Z. Cao, S. Dong, H. Jin, L. Sun, and J. Luo, "Analytical and experimental study of a valveless piezoelectric micropump with high flowrate and pressure load," *Microsystems & Nanoengineering*, vol. 9, 72, 2023. https://doi.org/10.1038/s41378-023-00547-7

Copyright © 2026 by the authors. This is an open access article distributed under the Creative Commons Attribution License which permits unrestricted use, distribution, and reproduction in any medium, provided the original work is properly cited (CC BY 4.0).